

PAPER

# Electrochemical phase diagrams of Ni from *ab initio* simulations: role of exchange interactions on accuracy

To cite this article: Liang-Feng Huang and James M Rondinelli 2017 *J. Phys.: Condens. Matter* **29** 475501

View the [article online](#) for updates and enhancements.

## Related content

- [Computational methods for 2D materials: discovery, property characterization, and application design](#)  
J T Paul, A K Singh, Z Dong et al.
- [First-principles determination of defect energy levels through hybrid density functionals and GW](#)  
Wei Chen and Alfredo Pasquarello
- [Improved electronic structure and magnetic exchange interactions in transition metal oxides](#)  
Priya Gopal, Riccardo De Gennaro, Marta Silva dos Santos Gusmao et al.

# Electrochemical phase diagrams of Ni from *ab initio* simulations: role of exchange interactions on accuracy

Liang-Feng Huang<sup>✉</sup> and James M Rondinelli<sup>✉</sup>

Department of Materials Science & Engineering, Northwestern University, Evanston, IL 60208, United States of America

E-mail: [jrondinelli@northwestern.edu](mailto:jrondinelli@northwestern.edu)

Received 7 August 2017, revised 3 October 2017

Accepted for publication 5 October 2017

Published 31 October 2017




CrossMark

## Abstract

The stabilities of Ni metal and its derived compounds, including oxides, hydroxides, and oxyhydroxides under electrochemical conditions, can be readily predicted from the Ni Pourbaix diagram, where the formation free energies of the involved species are utilized to construct the phase stability map with respect to electrode potential and pH. We calculate and analyze the crystal structures, electronic structures, and thermodynamic energies of Ni metal and its compounds using different exchange-correlation functionals to density-functional-theory (DFT), including the semilocal LDA and GGA density functionals, the nonlocal metaGGA, and the hybrid density functionals. Next, we simulate the corresponding Ni Pourbaix diagrams to compare systematically the performance of the functional to each other and to experimental observations. We show that the structures and energies obtained from experimental databases may not be sufficiently accurate to describe direct electrochemical observations, and we explain how the electronic exchange within the density functionals plays a key role in determining the accuracy of the DFT calculated electronic, thermodynamic, and electrochemical properties. We find that only the hybrid density functional produces reliable results owing to the fractional contribution of exact Fock exchange included therein. Last, based on our accurate Ni Pourbaix diagram, we construct band-gap and magnetic electrochemical maps which can facilitate more experimental measurements and property assessments under variable potential and pH in the future.

Keywords: nickel, Pourbaix diagram, corrosion, density functional theory

 Supplementary material for this article is available [online](#)

(Some figures may appear in colour only in the online journal)

## 1. Introduction

Elemental Ni metal and its alloys, compounds, and composite materials find broad applications in numerous civilian, industrial, and military fields, where their various superior properties are exploited: (1) corrosion-resistant biological Ni-alloy implants [1–3], which have more recently been replaced in part by  $\beta$ -Ti alloys with better mechanical and toxicologic biocompatibilities [4–6]; (2) superstrong and oxidation-resistant Ni alloys (e.g. Inconel) and coating ceramics (e.g.

NiCoCrAlY) for gas turbines [7–11]; (3) irradiation-resistant Ni alloys in nuclear reactors [12, 13]; (4) Invar alloys for precision instruments [14, 15]; (5) NiO-based resistive logic devices [16–19]; (6) metal-oxide-metal diodes [20]; (7) switchable mirrors made of Mg-Ni and Pd-Ni alloys [21] with optical properties sensitive to hydrogenation; (8) anode materials for solid oxide fuel cells (e.g. Ni/YZO) [22–24], lithium-ion batteries (e.g. Ni/NiO) [25–28], and capacitors (e.g. Ni/Ni(OH)<sub>2</sub> and Ni(OH)<sub>2</sub>/Cu<sub>2</sub>O/CuO) [29–32]; and (9) catalysts (e.g. NiO/NiAl<sub>2</sub>O<sub>4</sub>, Ni(OH)<sub>2</sub>, NiOOH, and Ni) [33–39].

The electrochemical properties of these Ni-based materials operating in any aqueous or humid environment is critical to the ultimate performance and life time of the material and device.

Pourbaix diagrams [40] can be used to describe the electrochemical stabilities of a metal and its compounds [41–43], defects in bulk solids [44–46], and adsorbates on surfaces [41, 47] at any electrode potential and solution pH. The Pourbaix diagram for elemental Ni, for example, readily indicates the electrochemical stabilities of Ni metal, oxides, hydroxides, and oxyhydroxides against dissolution into aqueous ions, which are also prerequisite for further understanding of the electrochemical effects of other additives in a variety of the aforementioned multicomponent Ni alloys and compounds. Although Ni Pourbaix diagrams have been simulated for over fifty years [40, 48–50], the electrochemical stabilities for NiO and Ni(OH)<sub>2</sub> derived from those diagrams are frequently inconsistent with various electrochemical observations [51]. This discrepancy has recently been attributed to underlying inaccuracies in the experimental formation free energies used to simulate the diagram, which may arise from defects and impurities in the samples and complexities in the experimental measurements [51]. On the contrary, reliable Ni Pourbaix diagrams have been derived from the formation free energies calculated using high-level density-functional theory (DFT) methods (i.e. hybrid functionals) [51]. These DFT Ni Pourbaix diagrams also have been closely validated by the experimental measurements using electrochemical impedance spectroscopy and surface-enhanced Raman spectroscopy, where the electrochemical stabilities of the passivating NiO and Ni(OH)<sub>2</sub> layers grown on the Ni samples exposed to different buffer solutions (pH 2.9–14) were characterized [51].

The aforementioned high-level hybrid DFT method is accurate, but remains computationally expensive. Many other exchange-correlation functionals to DFT provide increased efficiency, e.g. LDA, GGA, and metaGGA methods [52], albeit at the usual expense of accuracy in properties. Because materials physicists prefer to simulate material properties as accurately and efficiently as possible, it is important to assess which tier of density functional theory provides an optimal compromise to realize reliable and fast materials predictions. Understanding where the different accuracies in the thermodynamic and electrochemical properties of a material family with nontrivial interactions, i.e. Ni metal and its compounds, originate will be useful for both studying and predicting the the thermodynamic and electrochemical properties of known and new transition-metal materials and for the development of more advanced DFT methods.

In this work, we compute the equilibrium crystal structures, electronic structures, thermodynamic energies, and electrochemical stabilities of Ni metal and its oxides, hydroxide, and oxyhydroxide using density-functional theory with different tiers of exchange-correlation potentials ( $V_{xc}$ ). Our results and electronic-structure analyses show that the accuracy of a  $V_{xc}$  sensitively depends on nature of the electronic exchange potential. Property accuracy, relative to experiment, generally increases from semilocal LDA/GGA methods to nonlocal metaGGA and hybrid methods owing to the improved approximation for the electronic exchange interaction. We find that

only the hybrid DFT method, which includes exact Fock-exchange, can produce reliable Ni Pourbaix diagrams when compared to direct electrochemical phenomena observed in experiment. Last, we predict electrochemical maps parameterized in terms of electronic band gaps and long-range magnetic order, which suggest other possible experimental characterization probes to assess phase stability with variable potential and pH.

## 2. Methodology

### 2.1. Thermodynamic basis

The DFT formation energy ( $E_f$ ) of a Ni compound (e.g. Ni<sub>x</sub>O<sub>y</sub>H<sub>z</sub>) is calculated using

$$E_f = E_e(\text{Ni}_x\text{O}_y\text{H}_z) - xE_e(\text{Ni}) - \frac{y}{2}E_e(\text{O}_2) - \frac{z}{2}E_e(\text{H}_2), \quad (1)$$

where  $x$ ,  $y$ , and  $z$  are the number of Ni, O, and H atoms in a formula unit, respectively;  $E_e$  is the total electronic energy; and elemental Ni (FCC phase), O<sub>2</sub> molecule, and H<sub>2</sub> molecule are the references. At finite temperatures, the total free energy ( $G_{\text{tot}}$ ) of a solid or a molecular gas is expressed as

$$G_{\text{tot}}(T) = E_e + G_T(T), \quad (2)$$

where  $G_T$  includes temperature-dependent contributions from atomic vibrations and electronic excitations as well as molecular rotation and translation for O<sub>2</sub> and H<sub>2</sub> gases. The electronic free energies are negligibly small here, e.g.  $-2$  meV for Ni at 298.15 K. The standard O<sub>2</sub> and H<sub>2</sub> gases at 298.15 K and 1.0 bar are used as the references. The formation free energy ( $G_f$ ) of a Ni compound is calculated using

$$G_f(T) = E_f + \Delta G_T(T), \quad (3)$$

where  $\Delta G_T$  is calculated in a similar way as equation (1), with  $E_e$  therein replaced by  $G_T$ . The temperature-dependent  $\Delta G_T$  values are calculated in our previous work and used here [51].

For solids, the standard chemical potential  $\mu^s = G_f$ . For aqueous ions, the concentration-dependent chemical potential ( $\mu^l$ ) is calculated using

$$\mu^l = \mu_0^l + RT \ln([I]), \quad (4)$$

where  $R$  is the gas constant (8.314 J mol<sup>-1</sup> K<sup>-1</sup>);  $\mu_0^l$  is the chemical potential of ion  $I$  at the standard-solution condition (298.15 K, 1.0 bar, 1.0 mol L<sup>-1</sup>, and pH 0); and  $[I]$  is the aqueous-ion activity and approximated to be the concentration. The  $\mu_0^l$  values for the considered aqueous ions are obtained from experimental databases [40, 48, 53, 54]. In addition, the  $\mu_0$  of liquid H<sub>2</sub>O is  $-2.458$  eV per formula unit [55], and assumed to be constant.

In aqueous environments, the relative electrochemical stabilities between various species (e.g. metal, oxides, hydroxide, oxyhydroxide, and aqueous ions) are described by the reaction chemical potentials ( $\Delta\mu$ ) for the reaction paths that connect all the considered species using the previously defined  $\mu^s$ ,  $\mu^l$ , and  $\mu_0(\text{H}_2\text{O})$  values. The reaction paths used here and the corresponding reaction chemical potentials are listed in

**Table 1.** Reaction paths and reaction chemical potentials ( $\Delta\mu$ ), where  $F$  is the Faraday constant.

Reaction path	$\Delta\mu$
$\text{Ni} \rightarrow \text{Ni}^{2+} + 2e^-$	$\Delta\mu(\text{Ni} - \text{Ni}^{2+}) = -\mu(\text{Ni}^{2+}) + 2FV_{\text{SHE}}$
$\text{Ni}^{3+} + e^- \rightarrow \text{Ni}^{2+}$	$\Delta\mu(\text{Ni}^{3+} - \text{Ni}^{2+}) = \mu(\text{Ni}^{3+}) - \mu(\text{Ni}^{2+}) - FV_{\text{SHE}}$
$\text{NiOH}^+ + \text{H}^+ \rightarrow \text{Ni}^{2+} + \text{H}_2\text{O}$	$\Delta\mu(\text{NiOH}^+ - \text{Ni}^{2+}) = \mu(\text{NiOH}^+) - \mu(\text{Ni}^{2+}) - \mu(\text{H}_2\text{O}) - RT \ln(10) \cdot \text{pH}$
$\text{Ni}(\text{OH})_2 + 2\text{H}^+ \rightarrow \text{Ni}^{2+} + 2\text{H}_2\text{O}$	$\Delta\mu(\text{Ni}(\text{OH})_2 - \text{Ni}^{2+}) = \mu(\text{Ni}(\text{OH})_2) - \mu(\text{Ni}^{2+}) - 2\mu(\text{H}_2\text{O}) - 2RT \ln(10) \cdot \text{pH}$
$\text{Ni}(\text{OH})_3^- + 3\text{H}^+ \rightarrow \text{Ni}^{2+} + 3\text{H}_2\text{O}$	$\Delta\mu(\text{Ni}(\text{OH})_3^- - \text{Ni}^{2+}) = \mu(\text{Ni}(\text{OH})_3^-) - \mu(\text{Ni}^{2+}) - 3\mu(\text{H}_2\text{O}) - 3RT \ln(10) \cdot \text{pH}$
$\text{Ni}(\text{OH})_4^{2-} + 4\text{H}^+ \rightarrow \text{Ni}^{2+} + 4\text{H}_2\text{O}$	$\Delta\mu(\text{Ni}(\text{OH})_4^{2-} - \text{Ni}^{2+}) = \mu(\text{Ni}(\text{OH})_4^{2-}) - \mu(\text{Ni}^{2+}) - 4\mu(\text{H}_2\text{O}) - 4RT \ln(10) \cdot \text{pH}$
$\text{NiOOH} + 3\text{H}^+ + e^- \rightarrow \text{Ni}^{2+} + 2\text{H}_2\text{O}$	$\Delta\mu(\text{NiOOH} - \text{Ni}^{2+}) = \mu(\text{NiOOH}) - \mu(\text{Ni}^{2+}) - 2\mu(\text{H}_2\text{O}) - 3RT \ln(10) \cdot \text{pH} - FV_{\text{SHE}}$
$\text{NiO} + 2\text{H}^+ \rightarrow \text{Ni}^{2+} + \text{H}_2\text{O}$	$\Delta\mu(\text{NiO} - \text{Ni}^{2+}) = \mu(\text{NiO}) - \mu(\text{Ni}^{2+}) - \mu(\text{H}_2\text{O}) - 2RT \ln(10) \cdot \text{pH}$
$\frac{1}{3}\text{Ni}_3\text{O}_4 + \frac{8}{3}\text{H}^+ + \frac{2}{3}e^- \rightarrow \text{Ni}^{2+} + \frac{4}{3}\text{H}_2\text{O}$	$\Delta\mu(\text{Ni}_3\text{O}_4 - \text{Ni}^{2+}) = \frac{1}{3}\mu(\text{Ni}_3\text{O}_4) - \mu(\text{Ni}^{2+}) - \frac{4}{3}\mu(\text{H}_2\text{O}) - \frac{8}{3}RT \ln(10) \cdot \text{pH} - \frac{2}{3}FV_{\text{SHE}}$
$\frac{1}{2}\text{Ni}_2\text{O}_3 + 3\text{H}^+ + e^- \rightarrow \text{Ni}^{2+} + \frac{3}{2}\text{H}_2\text{O}$	$\Delta\mu(\text{Ni}_2\text{O}_3 - \text{Ni}^{2+}) = \frac{1}{2}\mu(\text{Ni}_2\text{O}_3) - \mu(\text{Ni}^{2+}) - \frac{3}{2}\mu(\text{H}_2\text{O}) - 3RT \ln(10) \cdot \text{pH} - FV_{\text{SHE}}$
$\text{NiO}_2 + 4\text{H}^+ + 2e^- \rightarrow \text{Ni}^{2+} + 2\text{H}_2\text{O}$	$\Delta\mu(\text{NiO}_2 - \text{Ni}^{2+}) = \mu(\text{NiO}_2) - \mu(\text{Ni}^{2+}) - 2\mu(\text{H}_2\text{O}) - 4RT \ln(10) \cdot \text{pH} - 2FV_{\text{SHE}}$

table 1, where the standard hydrogen electrode (SHE) is used as the reference for the electrode potential ( $V_{\text{SHE}}$ ). The phase space spanned by  $V_{\text{SHE}} \in [-2, 3]$  V and solution  $\text{pH} \in [-2, 16]$  is accurately described by a dense homogeneous discrete grid (i.e.  $500 \times 500$ ). On each grid point, the relative stabilities of all the considered species are compared, and the lowest-energy phase or species identified [56], which finally leads to a Pourbaix diagram.

## 2.2. Density functionals

Various density functionals approximate the electronic exchange-correlation interaction at different levels of theory; they can be categorized into four tiers according to the Jacob's ladder [57]:

- (i) Local density approximation (LDA) functionals, where the exchange-correlation interaction at a local site equals that of a homogeneous electron gas with the same electron density;
- (ii) Generalized gradient approximation (GGA) functionals, where the electron density inhomogeneity (electron density gradient) is considered and 'corrects' the electronic exchange-correlation potential, e.g. PBE and PBEsol;
- (iii) MetaGGA functionals, where the electronic kinetic energy is specifically used to efficiently capture the nonlocal nature of electronic exchange interaction, e.g. RTPSS and MS2; and
- (iv) Hybrid functionals, where part of the semilocal GGA electronic exchange potential is replaced by the nonlocal exact Fock exchange potential, e.g. HSE06.

Owing to the difference in the scheme to approximate the electronic interaction, calculated materials properties exhibit different accuracy when compared to experiment. These density functionals generally (not always) exhibit an accuracy ranked as follow (from least to most accurate):  $\text{LDA} \lesssim \text{GGA} < \text{metaGGA} < \text{hybrid}$ ; similarly the most efficient functional is LDA, which is comparable to or faster than a GGA, followed by metaGGAs, and then hybrid functionals (least efficient). In this work, the CA [58] (LDA) functional, PBE [59, 60] and

PBEsol [61, 62] (GGA) functionals, RTPSS [63, 64] and MS2 [65, 66] (metaGGA) functionals, and HSE06 [67–71] (hybrid) functional are used. In PBEsol, the exchange-enhancement factor in PBE is modified to have the same asymptotic trend as that in LDA; therefore, PBEsol calculated energies always reside between those of PBE and LDA [56]. In HSE06, 25% short-range PBE electronic exchange is replaced by nonlocal Fock exchange, and a screening length of 9.4 Å is used for numerical convergence. Two reciprocal grids are required to describe the two-particle Fock electronic-exchange interaction [72], and to accurately calculate the screened nonlocal exchange, the second reciprocal grid (i.e.  $k^*$  grid) used in our HSE06 calculations is set to be  $\gtrsim \frac{a_0}{9.4} \times \frac{b_0}{9.4} \times \frac{c_0}{9.4}$  ( $a_0$ ,  $b_0$ , and  $c_0$  are lattice constants in Å) times that of the first reciprocal grid ( $k$  grid).

## 2.3. van der Waals correction

For systems with weak bonds (e.g. layered materials, rare gases, and molecular solids), the nonlocal van der Waals (vdW) interaction plays an important role in various properties, where a density functional with an optimized vdW correction can be used for simulation [73, 74]. There have been many methods proposed to calculate the vdW correction in DFT, which also have been comprehensively benchmarked for various metallic, ionic, covalent, and molecular solids [75–77]. These systematic studies have shown that the inter-layer bonding in layered materials such as graphite and h-BN can be well captured by those DFT-vdW methods; however, they still may not improve the DFT accuracy in many physical properties, e.g. lattice constants, bulk moduli, and energetics [75–77].

In this work,  $\text{NiO}_2$ ,  $\text{Ni}(\text{OH})_2$ , and  $\text{NiOOH}$  exhibit layered structures; for this reason, we will assess the effect of the vdW correction on their energies which can impact phase stability in the Pourbaix diagram. We consider four kinds of DFT-vdW methods: D2 (2006) [78], zero-damping D3 (2010) [79], Becke–Jonson-damping D3 (2011) [80], and self-consistent TS (2012) [81] methods, where the calculations are based on the PBE functional. The calculated vdW corrections to  $E_c$  and

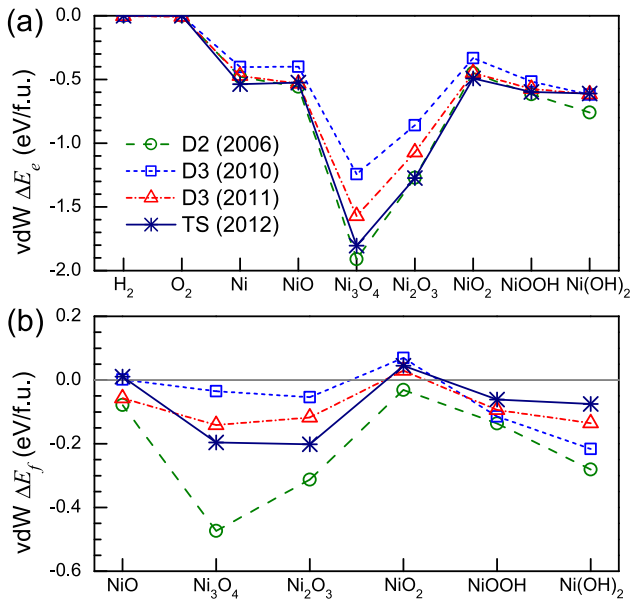


**Figure 1.** The vdW corrections to the (a) total electronic energies and (b) formation energies by four DFT-vdW methods.

$E_f$  ( $\text{vdW } \Delta E_e$  and  $\Delta E_f$ ) are shown in figure 1, which clearly exhibit two main features: (1) the magnitude of the DFT-vdW corrections differ remarkably from each other; and (2) the vdW formation energies,  $\Delta E_f$ , of the nonlayered solids ( $\text{NiO}$ ,  $\text{Ni}_2\text{O}_3$ , and  $\text{Ni}_3\text{O}_4$ ) are comparable to or even larger than those of the layered solids ( $\text{NiO}_2$ , NiOOH, and  $\text{Ni}(\text{OH})_2$ ), which should be a nonphysical consequence of using the DFT-vdW methods.

Therefore, to avoid any unnecessary complexity and unexpected uncertainty caused by using one of the DFT-vdW methods, we only consider the original DFT methods (free of vdW corrections) mentioned in the previous section throughout this work. We note that the strong hydrogen bonds may dominate the interlayer interaction in Ni (oxy) hydroxides [37, 39], and as we show later,  $\text{NiO}_2$  is only stabilized by a sufficiently high electrode potential where the weak vdW interlayer interaction ( $\sim 0.05$  eV/atom [75, 76]) cannot compete with the effect of the electrode potential (of an eV order or larger [56]).

#### 2.4. Self-interaction correction

There exists a self-interaction issue in conventional semilocal DFT functionals (e.g. LDA and GGA) [82, 83], i.e. the repulsive Hartree potential generated by an electron in a Kohn–Sham orbital is not fully cancelled by its own exchange–correlation potential. It may be severe for materials with spatially localized  $d$  or  $f$  orbitals [83–87] or localized impurity states [88, 89], where the on-site electronic repulsion is strong. As a consequence, many calculated physical properties (e.g. structure, band gap, magnetism, and elasticity) may exhibit significant inaccuracies. Self-interaction correction (SIC) schemes exist whereby the electronic-self potentials are subtracted from the functional using approximate formula [82–84, 86], and this can improve calculated physical properties for transition-metal

oxides (including NiO). Although SIC improves the performance of DFT for many materials with highly localized  $d$  or  $f$  orbitals, it may be inadequate for those with highly hybridized  $sp$  orbitals, e.g. Si, GeTe, and GaN [84, 85].

The spurious electronic self interaction can also be excluded by using the LDA+ $U$  (or DFT+ $U$ ) method, which has been widely used for various strongly-correlated materials [90]. In DFT+ $U$ , the mean-field Hartree–Fock approximation is used in the additional on-site Hubbard Hamiltonian, and there is no self-interaction issue in the exact Hartree–Fock potential. Thus, it can be naturally deduced that the self-interaction issue can be solved by increasing the portion of Hartree–Fock potential in a semilocal functional. However, the localized on-site  $U$  still is not optimally suited for materials with considerable interorbital hybridization and interatomic bonding (e.g. Si and GaAs), and accurate properties may only be obtained when a nonlocal Hubbard Hamiltonian  $V$  is used [91]. Surprisingly, such nonlocal  $V$  is also important for accurately calculating NiO, a correlated insulator, where both the localized Ni-3 $d$  and delocalized  $sp$  orbitals play important roles in the electronic structure.

Therefore, the use of an accurate nonlocal exchange potential may not only exclude the self-interaction issue, but also capture the nonlocal electronic character. In the HSE06 functional [67–71], these two purposes are achieved at the same time by partially using the exact Hartree–Fock potential, which should largely improve the DFT accuracy when dynamical correlations are not dominate (e.g. in 5 $f$ -electron materials [92]). Although in metaGGA functionals (e.g. RTPSS [63, 64] and MS2 [65, 66]), the nonlocal exchange potential is approximated by using electronic kinetic energy, their performances are still dependent on the potential accuracy.

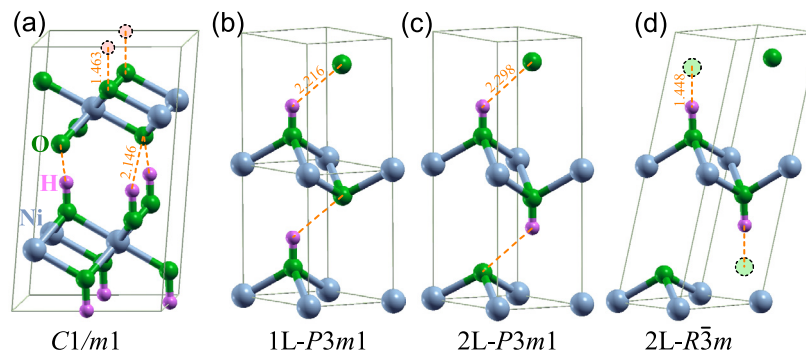
#### 2.5. Computational parameters

The DFT calculations are carried out using the Vienna *Ab Initio* Simulation Package [52]. The projector augmented-wave (PAW) method is used to describe the electronic wavefunction and Hamiltonian [93, 94]. The pseudopotentials of Ni, O, and H have valence configurations (ion radii) of  $3d^8 4s^2$  (2.30 bohr),  $2s^2 2p^4$  (1.52 bohr), and  $1s^1$  (1.10 bohr), respectively. To achieve an energy convergence of less than 1.0 meV/atom, the cutoff energy is set to be as high as 600 eV, which is mainly required by the O PAW pseudopotential. The reciprocal  $k$  grid is  $\gtrsim \frac{20}{a_0} \times \frac{20}{b_0} \times \frac{20}{c_0}$  for the Ni compounds and  $12 \times 12 \times 12$  for Ni metal. The energy and force convergence thresholds for the self-consistent electronic iteration are  $10^{-7}$  eV and  $10^{-3}$  eV  $\text{\AA}^{-1}$ , respectively, which are required to obtain accurate forces and stresses.

All functionals, LDA, PBE, PBEsol, RTPSS, MS2, and HSE06, are used to calculate the DFT formation energy (i.e.  $E_f$ ). Because the free energy  $G_T$  always exhibits a much weaker dependence on the density functional [56], we only use the PBEsol functional to calculate the vibrational energy contribution to  $G_T$  at 298.15 K since it has been shown to be sufficiently accurate. In other words, only the PBEsol functional is used to calculate the temperature dependence in the free energy.

**Table 2.** The formation energies ( $E_f$ ) per formula unit for Ni compounds calculated using various DFT functionals. The space groups (numbers in parentheses) for each compound are obtained from the ICSD [95] and those used in this work are also given.

Species	Space group (no.)		$E_f$ (eV/f.u.)					
	ICSD [95]	This work	LDA	PBE	PBEsol	RTPSS	MS2	HSE06
NiO	$Fm\bar{3}m$ (225)	$R\bar{3}m$ (166)	-1.675	-1.307	-1.355	-1.477	-2.376	-2.965
Ni <sub>3</sub> O <sub>4</sub>	$Fd\bar{3}m$ (227)	$Fd\bar{3}m$ (227)	-8.058	-5.804	-6.324	-5.622	-8.049	-8.147
Ni <sub>2</sub> O <sub>3</sub>	$R\bar{3}c$ (167)	$R\bar{3}c$ (167)	-5.755	-3.939	-4.443	-3.954	-5.730	-4.979
NiO <sub>2</sub>	$C12/m1$ (12)	$C12/m1$ (12)	-3.075	-2.125	-2.230	-2.092	-3.081	-1.997
NiO <sub>2</sub>	$P\bar{3}m1$ (164)	$P\bar{3}m1$ (164)	-3.088	-2.117	-2.363	-2.082	-3.074	-1.994
Ni(OH) <sub>2</sub>	$P\bar{3}m1$ (164)	$P\bar{3}m1$ (164)	-5.243	-4.186	-4.421	-3.820	-5.276	-6.238
Ni(OH) <sub>2</sub>	—	$P\bar{3}$ (147)	-5.250	-4.184	-4.424	-3.823	-5.277	-6.234
NiOOH	$C12/m1$ (12)	$C1/m1$ (8)	-4.579	-3.368	-3.688	-3.110	-4.280	-4.152
NiOOH(1L)	$P3m1$ (156)	$P3m1$ (156)	-4.358	-3.147	-3.470	-2.911	-4.034	-3.996
NiOOH(2L)	—	$P3m1$ (156)	-4.445	-3.284	-3.583	-3.062	-4.223	-4.119
NiOOH(2L)	—	$R\bar{3}m$ (166)	-4.718	-3.458	-3.809	-3.184	-4.356	-4.224

**Figure 2.** The structures of the (a)  $C1/m1$ , (b)  $1L-P3m1$ , (c)  $2L-P3m1$ , and (d)  $2L-R\bar{3}m$  phases of NiOOH, where the unit cells are indicated by parallelepipeds and the hydrogen bonds (bond length in Å) are indicated by orange dashed lines. The positions of H atoms in (a) and O atoms in (d) in the neighboring unit cells are also indicated by dashed circles. Bond lengths presented are for the HSE06 functional; additional structural information may be found in the supplemental material<sup>1</sup>.

Except for a new structure for Ni(OH)<sub>2</sub> (space group  $P\bar{3}$ , No. 147) reported here, we use the formation free energy differences,  $\Delta G_f$ , for the Ni compounds reported in our previous work [51]. Throughout the manuscript, the formation free energies and Pourbaix diagrams will be referred to by the density functional used to calculate  $E_f$  despite vibrational free energies included in  $\Delta G_f$  being obtained from PBEsol-level calculations.

### 3. Results and discussion

#### 3.1. Crystal structures

Before discussing the thermodynamic, electronic, and electrochemical properties of the Ni compounds, we examine their structures in detail. The initial structures for the considered Ni oxides (NiO, Ni<sub>3</sub>O<sub>4</sub>, Ni<sub>2</sub>O<sub>3</sub>, and NiO<sub>2</sub>), hydroxide Ni(OH)<sub>2</sub>, and oxyhydroxide NiOOH are obtained from the *inorganic crystal structure database* (ICSD) [95], and the lattice constants and atomic positions for each structure further optimized using all aforementioned density functionals. The space group symmetries for all structures obtained from ICSD

and those calculated in this work are listed table 2. There are no experimental structures for Ni<sub>3</sub>O<sub>4</sub> and Ni<sub>2</sub>O<sub>3</sub> archived in ICSD; therefore, we used those of Fe<sub>3</sub>O<sub>4</sub> and Fe<sub>2</sub>O<sub>3</sub> as the initial structures for the DFT variable-cell and atom relaxations. In the reported  $P\bar{3}m1$  Ni(OH)<sub>2</sub> structure, there is a buckled hexagonal NiO<sub>2</sub> layer fully saturated by H atoms on two sides; by removing one and two H atoms, we obtain  $P3m1$  NiOOH ( $1L-P3m1$  NiOOH shown in figure 2(b)) and  $P\bar{3}m1$  NiO<sub>2</sub>, respectively.

The ICSD entry for NiO ( $Fm\bar{3}m$  symmetry, table 2) indicates it exhibits a perfect rock-salt structure, while our DFT structural optimization finds a small rhombohedral distortion which reduces the symmetry to  $R\bar{3}m$ . This rhombohedral structure is close to the ideal structure, and has been widely observed in many experimental [96, 97] and theoretical studies [98, 99]. Our DFT structure relaxations do not find alternate symmetries for Ni<sub>3</sub>O<sub>4</sub>, Ni<sub>2</sub>O<sub>3</sub>, and NiO<sub>2</sub>, where Ni<sub>3</sub>O<sub>4</sub> may be described as defective NiO lattice with ordered Ni vacancies.

The  $C1/m1$  phase of NiOOH consists of two alternating NiO<sub>2</sub> and Ni(OH)<sub>2</sub> layers with two different hydrogen bond lengths of 1.463 and 2.146 Å, respectively (figure 2(a)). In contrast, the  $1L-P3m1$  variant of NiOOH consists of only one NiOOH layer (i.e. NiO<sub>2</sub> half saturated by H), and has a single hydrogen bond length of 2.216 Å (figure 2(b)).  $C1/m1$  NiOOH

<sup>1</sup> See footnote 2.

has a lower  $E_f$  than that of 1L- $P3m1$  NiOOH by 0.16–0.25 eV f.u.<sup>-1</sup> (table 2), which may originate from both the partially enhanced hydrogen bonds and the optimized hydrogen saturation configuration in the former.

Based on 1L- $P3m1$  NiOOH, we further construct another NiOOH polymorph consisting of alternating NiO<sub>2</sub> and Ni(OH)<sub>2</sub> layers (2L- $P3m1$  NiOOH in figure 2(c)). The  $E_f$  for this structure is 0.11–0.19 eV f.u.<sup>-1</sup> lower than that of 1L- $P3m1$  NiOOH, although there is no significant change in the hydrogen-bond length (2.298 Å). This finding indicates that the NiOOH structure with such alternating H saturation configuration is more energetically favored. We note that when the symmetry constraint is removed during the DFT structural optimization of the 2L- $P3m1$  NiOOH phase, the unit cell spontaneously shears (figure 2(d)) with an increase in symmetry to  $R\bar{3}m$  (see table 2) and its formation energy is further lowered by 0.11–0.27 eV f.u.<sup>-1</sup>. In the  $C1/m1$ , 1L- $P3m1$ , and 2L- $P3m1$  NiOOH structures, the hexagonal Ni layers exhibit *AB*, *AA*, and *AA* stacking, respectively, while, in the 2L- $R\bar{3}m$  NiOOH structure, the change in the interaxial angles requires an *ABC* stacking and a shorter fully optimized hydrogen bond length (1.448 Å). Thus, apart from the optimized hydrogen-saturation configuration, the hydrogen-bond enhancement also makes a positive contribution to the stability of NiOOH. These results indicate that structures obtained from existing databases may lead to incorrect formation energies, and as we find DFT structural optimizations can produce energy variations of several tenths of electronvolts per formula unit. Selection of the structures used in first-principles thermodynamic calculations should therefore be carefully performed and reported.

Furthermore, based on the phonon spectra of  $P\bar{3}m1$  Ni(OH)<sub>2</sub>, we find a possible minor modulation of Ni(OH)<sub>2</sub> which would produce a  $3 \times 3 \times 1$  superstructure, whereby a lateral displacement of H atoms (by 0.2 Å) lowers the structural symmetry to  $P\bar{3}$  (see supplemental material<sup>2</sup>). However, these two phases of Ni(OH)<sub>2</sub> have nearly the same formation energies (table 2) and vibrational free energies (see supplemental material<sup>3</sup>). Such structural modulation can optimize the spatial configuration of the dipolar O–H bonds therein; however, for the present analysis focused on the thermodynamics of Ni(OH)<sub>2</sub>, it is unlikely to be important.

### 3.2. Thermodynamics and electronic structures

The formation energies ( $E_f$ ) per atom calculated using different DFT functional are presented in figure 3(a), and the detailed data (in eV per formula unit) are listed in table 2. It has been known in experiment for decades that NiO is the most stable among all Ni oxides [40, 48, 54, 100, 101], which is reproduced by both the MS2 and HSE06 functionals giving the lowest  $E_f$  per atom at NiO (figure 3(a)). However, LDA, PBE, PBEsol, and RTPSS all incorrectly assign the lowest

<sup>2</sup> See supplemental material at ([stacks.iop.org/JPhysCM/29/475501/mmedia](http://stacks.iop.org/JPhysCM/29/475501/mmedia)) for the structures of Ni compounds from different DFT methods, dynamical modulation of the structure of Ni(OH)<sub>2</sub>, and two possible magnetic configurations of NiOOH.

<sup>3</sup> See footnote 2.

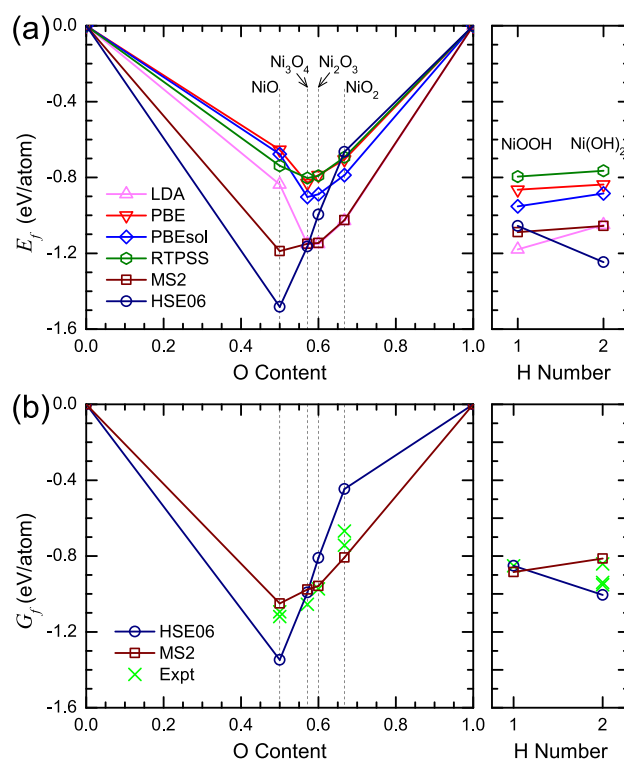


**Figure 3.** (a) Formation energies ( $E_f$ ) per atom from various DFT methods and (b) MS2, HSE06, and experimental formation free energies ( $G_f$ ) per atom for Ni compounds. More numerical details can be found in table 2.

formation energy to Ni<sub>3</sub>O<sub>4</sub>, which means that NiO exhibits an incorrect thermodynamic transition tendency into a ‘Ni+Ni<sub>3</sub>O<sub>4</sub>’ complex. The  $E_f$  per atom of Ni(OH)<sub>2</sub> is lower than that of NiOOH by HSE06, which is reversed by other DFT methods.

In figure 3(b), the MS2 and HSE06 formation free energies ( $G_f$ ) at 298.15 K are compared with those estimated from experimental measurements. It should be noted that the experimental formation free energies are likely inaccurate as reported in [51]; the accuracy of the HSE06  $G_f$  values will be directly assessed by comparing the calculated Pourbaix diagrams with direct electrochemical data (see section 3.3). Both MS2 and HSE06 yield the same chemical trends as found in experiment for the Ni oxide formation free energies. Although the  $G_f$  values of NiOOH and Ni(OH)<sub>2</sub> obtained from MS2 and HSE06 exhibit different chemical trends, the scattered experimental data show a trend closer to that obtained from the HSE06 functional. Apart from these qualitative discrepancies among different density functionals, the quantitative differences in  $E_f$  (or  $G_f$ ) is also considerable ( $\lesssim 0.9$  eV/atom); for this reason, we next investigate in detail the underlying electronic origin of this behavior.

As mentioned in the methodology section, HSE06 includes nonlocal exact electronic exchange interactions among electrons with identical spin polarization, which can more accurately describe physical properties of many transition-metal oxides with localized *d* electrons (e.g. band gap, magnetism, lattice constants, dielectrics, and reaction energy) [33, 56, 98, 102–109]. MS2 improves the nonlocal electronic exchange

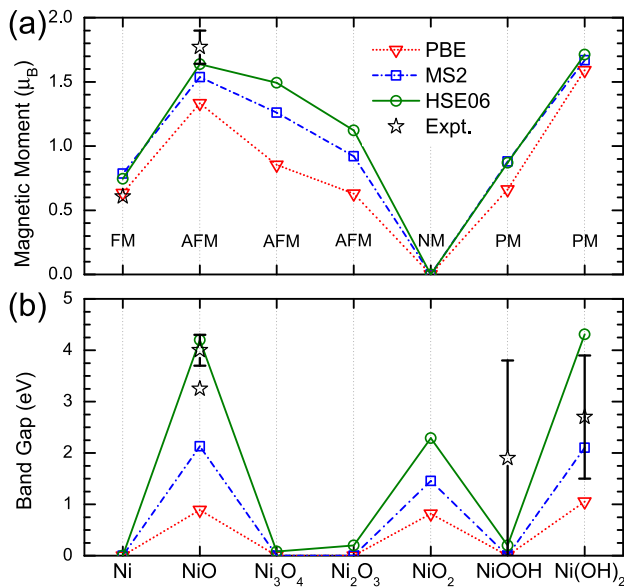


**Figure 4.** (a) Average magnetic moments on Ni atoms and (b) band gap ( $E_g$ ) value for Ni compounds from PBE, MS2, and HSE06, which are compared with the experimental results for the magnetic moment of Ni [110], magnetic moment and band gap of bulk NiO [111–117], and band gaps of NiO film (3.25 eV), NiOOH film (0–3.75 eV), and Ni(OH)<sub>2</sub> film (1.5–3.9 eV) [118, 119]. The magnetic configurations are indicated in panel (a), and the lines are guides to the eyes.

potential by additionally using electronic kinetic-energy density, which can more accurately describe the thermodynamic and electrochemical stability of Ti oxides [56].

The calculated average magnetic moments (on the Ni cations) and band gaps of the Ni compounds using PBE, MS2, and HSE06 are shown in figure 4, where the ferromagnetic (FM), antiferromagnetic (AFM), nonmagnetic (NM), and paramagnetic (PM) configurations are indicated. The available accurate experimental results for Ni and NiO, as well as some estimated experimental results for the band gaps of NiOOH and Ni(OH)<sub>2</sub> are collected for comparison. The hydrogenation degree in NiOOH and Ni(OH)<sub>2</sub> from experiment is not definitively known, and finite band gaps ( $\sim 3.8$  eV for both) are roughly estimated by extrapolating the measured photocurrent spectra, while the electrical conductivity of NiOOH indicates that it is metallic. Some in-gap states are also always measured in Ni(OH)<sub>2</sub> [118, 119]. Therefore, the measurement accuracy and sample quality may need to be improved to reduce the scatter in the experimental data for NiOOH and Ni(OH)<sub>2</sub> (figure 4(b)).

We also note because Ni<sub>3</sub>O<sub>4</sub> has a NiO lattice with ordered Ni vacancies, it strictly exhibits a ferrimagnetic state although it labeled as AFM due to the antiferromagnetic coupling between neighboring Ni atoms in figure 4. In the  $2 \times 2 \times 1$  supercells of Ni(OH)<sub>2</sub> and NiOOH, we find that the electronic energies of the AFM and FM spin configurations differ by  $\lesssim 4$  meV per Ni atom, suggesting a PM magnetic state at room temperature. More information about the magnetism in NiOOH and Ni(OH)<sub>2</sub> are given in the supplemental material<sup>4</sup>.

<sup>4</sup> See footnote 2.

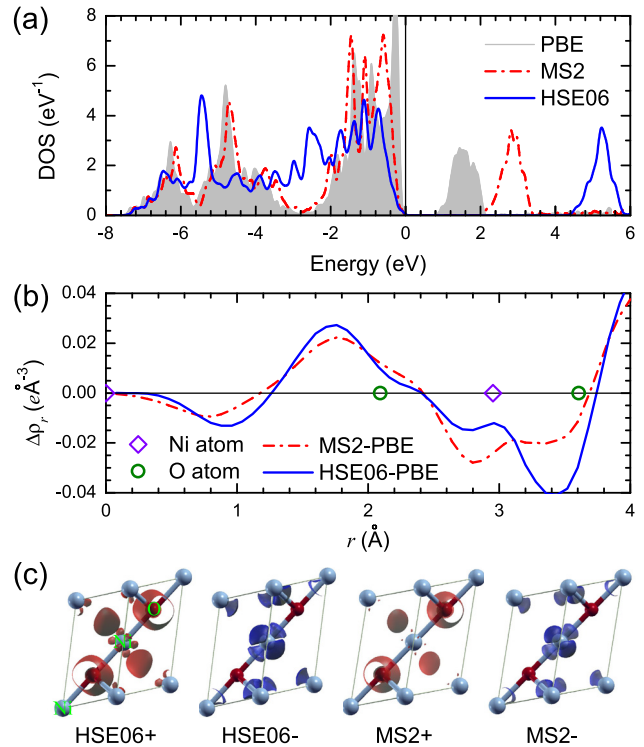


**Figure 5.** (a) Densities-of-states (DOS) of NiO from PBE, MS2, and HSE06, where the reference (0 eV) is shifted to be the highest occupied level. ((b) and (c)) Differential  $\rho_r(r)$  and  $\rho(\mathbf{r})$  values in NiO,  $\Delta\rho_r(r)$  and  $\Delta\rho(\mathbf{r})$ , with PBE  $\rho_r(r)$  and  $\rho(\mathbf{r})$  values as the references, respectively. In (b), the origin resides at a Ni atom; in (c), the electronic charges in a periodic unit cell of NiO are shown, and the isovalues are  $\pm 0.015 e \text{ \AA}^{-3}$  for the positive (HSE06+ and MS2+) and negative (HSE06- and MS2-) parts of  $\Delta\rho$ , respectively.

Our results to here show that HSE06 gives high and systematic accuracy among Ni compounds and that MS2 offers improved accuracy with respect to the PBE functional. The nonlocal exchange interaction between identical electrons is attractive, and tends to both decrease the energies of the occupied electrons and increase the atomic magnetic moments [72]. On the other hand, materials with higher atomic magnetic moments tend to have larger nonlocal exchange attractions and larger band gaps. For this reason, the HSE06 band gaps and magnetic moments are always the largest because it maximizes the exchange interactions. The exchange attraction should be weaker in MS2 and the weakest in the semi-local PBE; thus, the MS2 band gaps and magnetic moments always reside between the HSE06 and PBE values. It is this exchange attraction that make (i) the HSE06 and MS2  $E_f$ 's of NiO considerably lower than the LDA, PBE, PBEsol, and RTPSS ones, owing to the larger magnetic moments stabilized by the former two methods (figure 4(a)), and (ii) the HSE06  $E_f$  of Ni(OH)<sub>2</sub> is lower than that of NiOOH (figure 3(a)) owing again to the larger magnetic moment (exchange attraction) in Ni(OH)<sub>2</sub>. In addition, for compounds exhibiting magnetic ordering weaker than NiO and Ni(OH)<sub>2</sub>, the HSE06  $E_f$  values of these compounds are always reduced by less or even increased with respect to those from other DFT methods, because the electronic energies ( $E_e$ ) of the magnetic



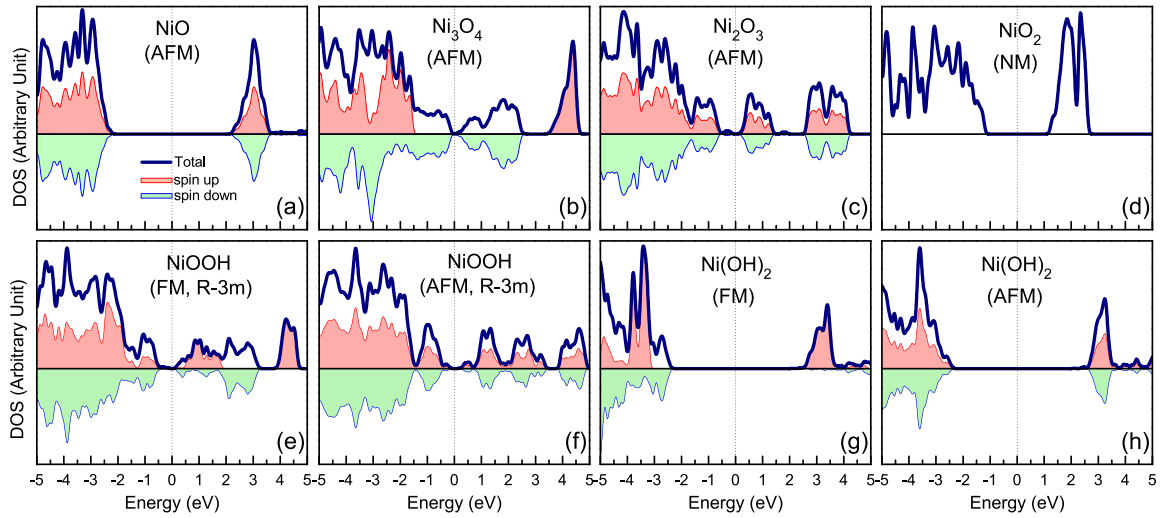


**Figure 6.** Densities-of-states of all NiO-based compounds calculated at the DFT-HSE06 level, where the reference energy level (0 eV) is the Fermi level (middle of the band gap) for conducting (insulating) compounds.

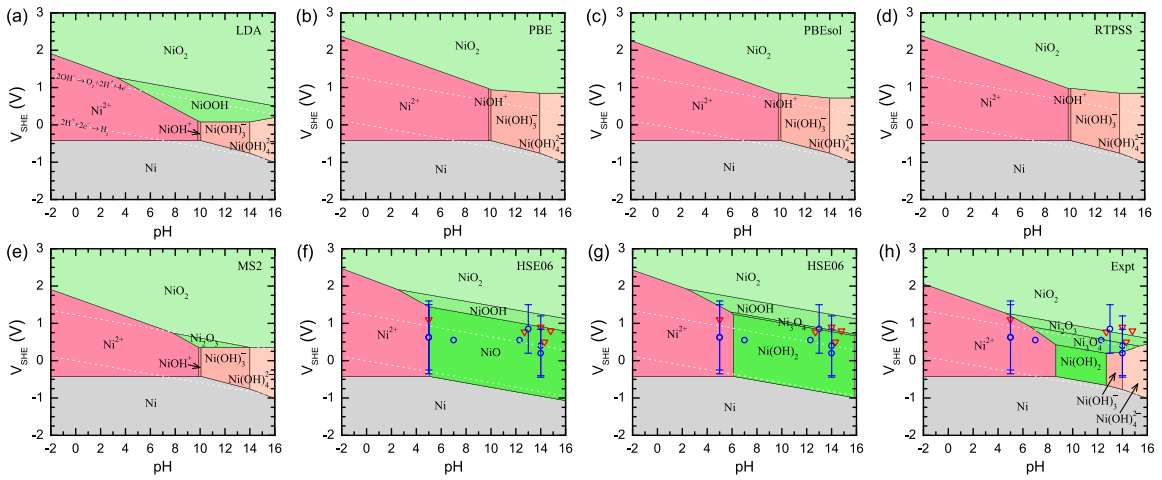


**Figure 7.** Calculated Ni Pourbaix diagrams at 298.15 K ( $[I] = 10^{-6} \text{ mol L}^{-1}$ ) constructed using various methods. The two (white ...) parallel lines correspond to the oxidation and reduction boundaries of water. Available experimental results [29–32, 35, 120–127] for the stabilities (blue  $\circ$ ) and average oxidation potentials (red  $\nabla$ ) of NiO and Ni(OH)<sub>2</sub> are summarized in panels ((f)–(h)), where the error bars on the symbols indicate the observed stability range.

Ni ( $\sim 0.7 \mu_B$ ) and O<sub>2</sub> ( $2.0 \mu_B$ ) references are also decreased by the nonlocal exchange attraction, which positively contributes to the formation energies in equation (1).

To clearly present the effect of nonlocal exchange interaction in the electronic structure, we further analyze the density-functional dependent density of states (DOS) and electronic density of AFM NiO (figure 5). In the DOS show in figure 5(a), we find that from PBE to MS2 and HSE06, the occupied and unoccupied states are shifted further and further away from each other, resulting in lower occupation (band) energies and increased band gaps ( $E_g$ ). This is consistent with the effect of nonlocal exchange attraction discussed above.

The radial average electron density ( $\rho_r$ ) is also used to facilitate the analysis [56], which is defined as

$$\rho_r = \frac{1}{4\pi r^2} \int_{|\mathbf{r}|=r} \mathbf{dr} \rho(\mathbf{r}), \quad (5)$$

where  $r$  is the length of the position vector  $\mathbf{r}$ , and  $\rho(\mathbf{r})$  is the electronic density at  $\mathbf{r}$ . The density-functional dependent differential  $\rho_r$  and  $\rho$  (i.e.  $\Delta\rho_r$  and  $\Delta\rho$ ) are shown in figures 5(b) and (c), respectively, where the PBE  $\rho_r$  and  $\rho$  values are used as the references. From PBE to HSE06 or PBE to MS2, there is a decrease in density for the relatively delocalized  $sp$  orbitals at the Ni sites indicated by the ‘HSE06 –’ or ‘MS2 –’  $\Delta\rho$  surface presented in figure 5(c). At the same time, the  $\rho$  for the localized  $d$  orbitals closer to the Ni nuclei and the delocalized  $sp$  orbitals at the O sites increase, which is indicated by the ‘HSE06+’ or ‘MS2+’  $\Delta\rho$  surfaces (figure 5(c)). These changes in electronic density tend to increase the local moments on the Ni sites and the ionicity of the Ni–O bonds. Such density-functional dependence on the electronic density distribution manifests in the ‘HSE06-PBE’ or ‘MS2-PBE’  $\Delta\rho_r$  traces (figure 5(b)), where the depletion of Ni- $sp$  electrons at  $r \sim 0.9 \text{ \AA}$  and the accumulation of O- $sp$

electrons at  $r \sim 1.7 \text{ \AA}$  is readily observed. At the Ni atom ( $0.0 \text{ \AA}$  along the abscissa), the rearrangement between  $d$  and  $sp$  electrons results in negligible  $\Delta\rho_r$  values there.

As described above, only the electronic structure of NiO has been systematically characterized in experiment. To facilitate any related experiment on Ni compounds in the future, the DOSs for all Ni-based oxides, oxyhydroxide, and hydroxide calculated from HSE06 functional are provided in figure 6. Owing to the possible PM state for NiOOH and Ni(OH)<sub>2</sub> in realistic conditions, the DOSs for their AFM and FM states are both given.

### 3.3. Ni Pourbaix diagrams

The Pourbaix diagrams at 298.15 K simulated using our theoretical formation free energies and the experimental  $G_f$  values are shown in figure 7, where we used the standard chemical potentials of aqueous ions measured in electrochemical experiments [40, 48, 53, 54] and a moderate aqueous-ion concentration [ $I$ ] of  $10^{-6} \text{ mol L}^{-1}$ . Panels (a)–(g) correspond to DFT calculated Pourbaix diagrams with different functionals indicated in the corner of each phase diagram; the Ni Pourbaix diagram constructed using the experimental  $G_f$  values is shown in figure 7(h).

The PBE, PBEsol, and RTPSS Pourbaix diagrams are quite similar with each other (figures 7(b)–(d)), which is expected because of the small differences in the calculated formation energies,  $E_f$  (see, figure 3(a)). The LDA, MS2, and HSE06 Pourbaix diagrams are shown in figures 7(a), (e) and (f), respectively. The relative electrochemical stabilities of the considered species with respect to electrode potential ( $V_{\text{SHE}}$ ) and solution pH are described by their reaction chemical potentials ( $\Delta\mu$ , table 1). The  $\Delta\mu$  of Ni(OH)<sub>2</sub> is higher than that of NiO by only  $\sim 0.13 \text{ eV}$  per Ni atom from HSE06, and the formation probabilities of each of these compounds in electrochemical experiments can be easily altered by some kinetic factors [51]. For this reason and to understand the electrochemical stability of Ni(OH)<sub>2</sub>, we exclude NiO to construct a metastable Pourbaix diagram in figure 7(g), which includes the metastable Ni(OH)<sub>2</sub> phase. Now figures 7(f) and (g) can be directly compared to show that the NiO phase field is largely replaced by Ni(OH)<sub>2</sub> in panel (g) and that the suppression of NiO allows Ni<sub>3</sub>O<sub>4</sub> to appear in a very narrow range of pH and potential.

The phase domains with stable metal, (hydr)oxides, and aqueous ions are called the *immunity*, *passivation*, and *corrosion* domains, respectively [40]. To prevent the corrosion of Ni, one should maintain the electrochemical condition within the immunity or passivation domain. In the later situation, the metal will be protected by a passivating layer (e.g. Ni(OH)<sub>2</sub> or/and NiO) formed on the surface, which is similar to the corrosion resistance mechanism for Ti in aqueous environments (i.e. TiO<sub>2</sub> protection) [56]. If a Ni metal or compound is stable outside the stability region of water, it may be a useful electrode material for some hydrolysis applications, e.g. generation of O<sub>2</sub> and H<sub>2</sub> gases by electrochemical or photocatalytic methods.

Prior to evaluating these simulated Pourbaix diagrams, various experimental electrochemical observations at room temperature should be introduced. In experiments, although Ni(OH)<sub>2</sub> is reported more frequently than NiO [29–31, 35, 127], possibly due to the lower kinetic barrier for the formation of Ni(OH)<sub>2</sub>, NiO may still coexist with Ni(OH)<sub>2</sub> [120–125]. The measured stability domains of NiO and Ni(OH)<sub>2</sub>, as well as their oxidation potentials (into NiOOH), are collected in figures 7(f)–(h). It should be noted that an experimental uncertainty of  $\lesssim 0.5 \text{ V}$  is also possible in the oxidation potential due to either kinetic factors or measurement uncertainty. Stable NiO and/or Ni(OH)<sub>2</sub> have been observed in solutions with pH of 5–14.8. Thus, Pourbaix diagrams obtained from LDA, PBE, PBEsol, RTPSS, and MS2 are obviously inconsistent with the experimental reality. The failure of these functionals is attributed to the relative stabilities of the passivating Ni compounds against dissolution being largely underestimated, indicating inaccuracy of the corresponding formation energies,  $E_f$ , in figure 3(a). In the Pourbaix diagram constructed using the experimental formation free energies, the passivating Ni(OH)<sub>2</sub> is found to only be stable at pH values of 9–13. This inconsistency in the range of stability indicates inaccuracies in the the experimental  $G_f$  values (figure 3(b)). Only the HSE06 Pourbaix diagrams are able to accurately reproduce the electrochemical stabilities and oxidation potentials for NiO and Ni(OH)<sub>2</sub>, indicating high accuracy of the HSE06 calculated formation energies and formation free energies (figures 3(a) and (b)).

The above accuracy evaluation for the Ni Pourbaix diagrams shows that (i) one can effectively assess the accuracy of thermodynamic energies by comparing simulated Pourbaix diagrams with direct electrochemical observations, and (ii) nonlocal-exchange interactions are an important ingredient to obtain accurate DFT thermodynamic energies and electrochemical phase diagrams. This knowledge should be useful for future *ab initio* simulations of thermodynamic and electrochemical stabilities of various transition metals and their compounds. We also suggest that the performance of any newly constructed density functionals (e.g. metaGGA SCAN by Sun *et al* [77, 128]), can be better benchmarked by assessing electrochemical [51, 56] and/or thermodynamic [6, 129] phase diagrams rather than through standard comparisons of energies indirectly obtained in experiment.

### 3.4. Potential–pH–property maps

Realizing that Ni metal and its compounds exhibit different band gaps and magnetic phases, as shown in figure 4, we further construct electrochemical maps with phase fields defined by the band gap or magnetic state. These potential–pH–property maps can facilitate alternative property measurements and exploitation in the future with variable pH (during, for example, a chemical reaction) or potential (cycling). Under an electrochemical condition, the globally averaged band gap ( $\bar{E}_g$ ) is calculated using

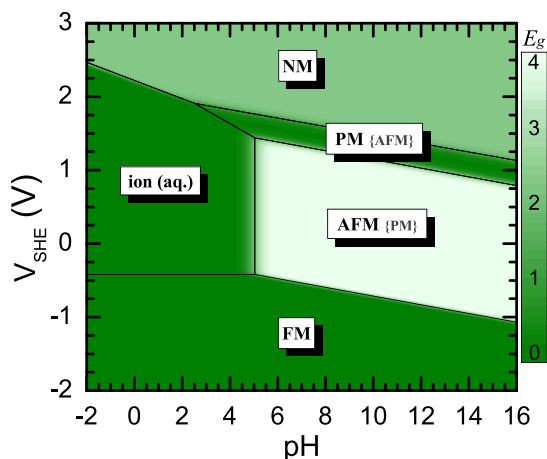


**Figure 8.** The maps of band gap ( $E_g$ , in eV) and magnetic state for the electrochemical products present in the Ni Pourbaix diagram (HSE06). The magnetic phases for metastable  $\text{Ni}(\text{OH})_2$  and  $\text{Ni}_3\text{O}_4$  are also indicated in the parentheses in the corresponding NiO and NiOOH domains, respectively.

$$\bar{E}_g = \sum_i E_g^i P_i = \sum_{i,j} E_g^i \frac{\exp(-\frac{\Delta\mu_i}{k_B T})}{\exp(-\frac{\Delta\mu_j}{k_B T})}, \quad (6)$$

where  $i$  and  $j$  index the species, and  $P_i$  is the electrochemical probability of the  $i$ th species. The  $E_g$  for the corrosion domain with stable aqueous ion is set to be 0.0 eV owing to the absence of any passivating layer on Ni metal.

The simulated variation of  $\bar{E}_g$  with respect to  $V_{\text{SHE}}$  and pH is shown in figure 8, and the magnetism map is indicated by the labeled magnetic state for the corresponding phase. We note again that ferrimagnetic  $\text{Ni}_3\text{O}_4$  is labeled as AFM for simplicity in this diagram. In the AFM NiO (PM NiOOH) domain, the magnetism for the metastable PM  $\text{Ni}(\text{OH})_2$  (AFM  $\text{Ni}_3\text{O}_4$ ) has a secondary probability and is also given [51].

In a solution with  $\text{pH} \in [5, 15]$ , both  $E_g$  and magnetism of the electrochemical product may change significantly with increasing  $V_{\text{SHE}}$ . This correlation between electrochemical condition and physical properties provides a possible way to realize electrochemically controllable  $E_g$  and magnetism, as well as many indirect experimental approaches to effectively characterize the electrochemical stability through property measurements rather than atomic structure fingerprinting. When a passivating Ni compound is formed on Ni metal under an electrochemical condition, for example, its band gap and magnetic state may be measured by various *ex/in situ* methods. The electronic gap of the passivating layers on metal could be measured by scanning tunneling microscopy [130], and the magnetism could be detected by scanning SQUID microscopy, magnetoresistance, and magneto-optics measurements [131–133].

#### 4. Conclusion

We used various exchange-correlation potentials to density functional theory to calculate the thermodynamic energies of Ni metal and its compounds, which were subsequently

used to construct the corresponding functional-dependent Ni Pourbaix diagrams. The thermodynamic and electrochemical accuracies of these DFT methods were comprehensively evaluated, and explained by an electronic-structure analysis. We found that the approximate scheme used to include electronic exchange in the potential is a key factor in determining accuracy with regards to reproducing electrochemical observations for magnetic compounds of Ni. The simulation accuracy tends to increase upon going from the semilocal LDA and GGA functionals to the nonlocal metaGGA and hybrid functionals owing to the increased electronic exchange attraction therein. In addition, we found that some crystal structures archived in widely used databases can be inconsistent with DFT calculations as shown for NiO and NiOOH. Last, we simulated electrochemical property maps, including band gap and magnetic state, for Ni and its compounds, which may facilitate future measurements and property applications.

#### Acknowledgments

L-FH and JMR thank Prof J R Scully, R J Santucci, and M Hutchison at University of Virginia, Prof L D Marks, Dr X-X Yu, and Mr E Tennesen at Northwestern University, and Dr G R Zhang at Institute of Solid State Physics, Chinese Academy of Sciences for helpful discussions. The authors were supported by the ONR MURI ‘Understanding Atomic Scale Structure in Four Dimensions to Design and Control Corrosion Resistant Alloys’ under Grant No. N00014-16-1-2280. Calculations were performed using the QUEST HPC Facility at Northwestern University, the HPCMP facilities at the Navy DSRC, the CARBON cluster at the Center for Nanoscale Materials in Argonne National Laboratory (DOE-BES, DE-AC02-06CH11357), and at the Extreme Science and Engineering Discovery Environment (NSF, ACI-1548562).

#### ORCID iDs

Liang-Feng Huang <https://orcid.org/0000-0003-2937-5183>  
James M Rondinelli <https://orcid.org/0000-0003-0508-2175>

#### References

- [1] Hoar T P and Mears D C 1966 Corrosion-resistant alloys in chloride solutions: materials for surgical implants *Proc. R. Soc. A* **294** 486–510
- [2] Pourbaix M 1984 *Biomaterials* **5** 122–34
- [3] Jacobs J J, Gilbert J L and Urban R M 1998 *J. Bone Joint Surg.* **80** 268–82
- [4] Niinomi M, Nakai M and Hieda J 2012 *Acta Biomater.* **8** 3888–903
- [5] Banerjee D and Williams J C 2013 *Acta Mater.* **61** 844–79
- [6] Huang L F, Grabowski B, Zhang J, Lai M J, Tazan C C, Sandlobes S, Raabe D and Neugebauer J 2016 *Acta Mater.* **113** 311–9
- [7] Goward G W 1998 *Surf. Coat. Technol.* **108–9** 73–9
- [8] Pature N P, Gell M and Jordan E H 2002 *Science* **296** 280–4

- [9] Eliaz N, Shemesh G and Latanision R M 2002 *Eng. Fail. Anal.* **9** 31–43
- [10] Pomeroy M J 2005 *Mater. Des.* **26** 223–31 (special issue: Tribology)
- [11] Xia P C, Chen F W, Xie K, Qiao L and Yu J J 2015 *Frontiers Mater. Sci.* **9** 85–92
- [12] Zinkle S J and Busby J T 2009 *Mater. Today* **12** 12–9
- [13] Zinkle S J and Snead L L 2014 *Annu. Rev. Mater. Res.* **44** 241–67
- [14] van Schilfgaarde M, Abrikosov I A and Johansson B 1999 *Nature* **400** 46–9
- [15] Yokoyama T and Eguchi K 2013 *Phys. Rev. Lett.* **110** 075901
- [16] Seo S *et al* 2004 *Appl. Phys. Lett.* **85** 5655–7
- [17] Waser R and Aono M 2007 *Nat. Mater.* **6** 833–40
- [18] Sawa A 2008 *Mater. Today* **11** 28–36
- [19] Calka P, Martinez E, Lafond D, Minoret S, Tirano S, Detlefs B, Roy J, Zegenhagen J and Guedj C 2011 *J. Appl. Phys.* **109** 124507
- [20] Wang K, Hu H, Lu S, Guo L and He T 2015 *Frontiers Phys.* **10** 1–12
- [21] Zhang X L, Bao S H, Xin Y C, Cao X and Jin P 2015 *Frontiers Mater. Sci.* **9** 227–33
- [22] Sarantaridis D and Atkinson A 2007 *Fuel Cells* **7** 246–58
- [23] Wang W, Su C, Wu Y, Ran R and Shao Z 2013 *Chem. Rev.* **113** 8104–51
- [24] Xu M, Li B, Wang B, Liu X, Li T S and Chen L 2015 *Electrochim. Acta* **167** 147–50
- [25] Poizat P, Laruelle S, Grugeon S, Dupont L and Tarascon J M 2000 *Nature* **407** 496–9
- [26] Aravindan V, Kumar P S, Sundaramurthy J, Ling W C, Ramakrishna S and Madhavi S 2013 *J. Power Sources* **227** 284–90
- [27] López M C, Ortiz G F, Lavela P and Tirado J L 2013 *J. Power Sources (16th Int. Meeting on Lithium Batteries)* **244** 403–9
- [28] Kvasha A, Azaceta E, Leonet O, Bengoechea M, Boyano I, Tena-Zaera R, de Meaza I, Miguel O, Grande H J and Blazquez J A 2015 *Electrochim. Acta* **180** 16–21
- [29] Wu Q, Wen M, Chen S and Wu Q 2015 *J. Alloy. Compd.* **646** 990–7
- [30] Chen J S, Gui Y and Blackwood D J 2016 *Electrochim. Acta* **188** 863–70
- [31] Abbas S A and Jung K D 2016 *Electrochim. Acta* **193** 145–53
- [32] Ruan J J, Huo Y Q and Hu B 2016 *Electrochim. Acta* **215** 108–13
- [33] Nolan M, Long R, English N J and Mooney D A 2011 *J. Chem. Phys.* **134** 224703
- [34] Wang J and Higashihara T 2014 *Frontiers Mater. Sci.* **8** 383–90
- [35] Qin M, Maza W A, Stratakes B M, Ahrenholtz S R, Morris A J and He Z 2016 *J. Electrochem. Soc.* **163** F437–42
- [36] Gao M, Sheng W, Zhuang Z, Fang Q, Gu S, Jiang J and Yan Y 2014 *J. Am. Chem. Soc.* **136** 7077–84
- [37] Li Y F and Selloni A 2014 *J. Phys. Chem. Lett.* **5** 3981–5
- [38] Burke M S, Zou S, Enman L J, Kellon J E, Gabor C A, Pledger E and Boettcher S W 2015 *J. Phys. Chem. Lett.* **6** 3737–42
- [39] Zaffran J and Caspary Toroker M 2016 *J. Chem. Theory Comput.* **12** 3807–12
- [40] Pourbaix M 1966 *ATLAS of Electrochemical Equilibria in Aqueous Solutions* (Oxford: Pergamon)
- [41] Persson K A, Waldwick B, Lazic P and Ceder G 2012 *Phys. Rev. B* **85** 235438
- [42] Castelli I E, Thygesen K S and Jacobsen K W 2014 *Top. Catal.* **57** 265–72
- [43] Zeng Z, Chan M K Y, Zhao Z J, Kubal J, Fan D and Greeley J 2015 *J. Phys. Chem. C* **119** 18177–87
- [44] Todorova M and Neugebauer J 2014 *Phys. Rev. Appl.* **1** 014001
- [45] Todorova M and Neugebauer J 2015 *Faraday Discuss.* **180** 97–112
- [46] Todorova M and Neugebauer J 2015 *Surf. Sci.* **631** 190–5
- [47] Hansen H A, Rossmeisl J and Nørskov J K 2008 *Phys. Chem. Chem. Phys.* **10** 3722–30
- [48] Beverskog B and Puigdomenech I 1997 *Corros. Sci.* **39** 969–80
- [49] Munoz-Portero M J, García-Antón J, Guinón J L and Pérez-Herranz V 2007 *Corrosion* **63** 625–34
- [50] Cook W G and Olive R P 2012 *Corros. Sci.* **58** 284–90
- [51] Huang L F, Hutchison M J, Santucci R J Jr, Scully J R and Rondinelli J M 2017 *J. Phys. Chem. C* **121** 9782–9
- [52] Hafner J 2008 *J. Comput. Chem.* **29** 2044–78
- [53] Burgess J 1978 *Metal Ions in Solution* (Chichester: Ellis Horwood)
- [54] Bard A J, Parsons R and Jordan J 1985 *Standard Potentials in Aqueous Solution* (New York: Marcel Dekker)
- [55] Chase M W 1998 *NIST-JANAF Thermochemical Tables* 4th edn (New York: American Institute of Physics)
- [56] Huang L F and Rondinelli J M 2015 *Phys. Rev. B* **92** 245126
- [57] Perdew J P and Schmidt K 2001 *AIP Conf. Proc.* **577** 1–20
- [58] Ceperley D M and Alder B J 1980 *Phys. Rev. Lett.* **45** 566–9
- [59] Perdew J P, Burke K and Ernzerhof M 1996 *Phys. Rev. Lett.* **77** 3865–8
- [60] Perdew J P, Burke K and Ernzerhof M 1997 *Phys. Rev. Lett.* **78** 1396–6
- [61] Perdew J P, Ruzsinszky A, Csonka G I, Vydrov O A, Scuseria G E, Constantin L A, Zhou X and Burke K 2008 *Phys. Rev. Lett.* **100** 136406
- [62] Perdew J P, Ruzsinszky A, Csonka G I, Vydrov O A, Scuseria G E, Constantin L A, Zhou X and Burke K 2009 *Phys. Rev. Lett.* **102** 039902
- [63] Tao J, Perdew J P, Staroverov V N and Scuseria G E 2003 *Phys. Rev. Lett.* **91** 146401
- [64] Perdew J P, Ruzsinszky A, Csonka G I, Constantin L A and Sun J 2009 *Phys. Rev. Lett.* **103** 026403
- [65] Sun J, Haunschild R, Xiao B, Bulik I W, Scuseria G E and Perdew J P 2013 *J. Chem. Phys.* **138** 044113
- [66] Sun J, Xiao B, Fang Y, Haunschild R, Hao P, Ruzsinszky A, Csonka G I, Scuseria G E and Perdew J P 2013 *Phys. Rev. Lett.* **111** 106401
- [67] Heyd J, Scuseria G E and Ernzerhof M 2003 *J. Chem. Phys.* **118** 8207–15
- [68] Heyd J and Scuseria G E 2004 *J. Chem. Phys.* **120** 7274–80
- [69] Heyd J and Scuseria G E 2004 *J. Chem. Phys.* **121** 1187–92
- [70] Heyd J, Scuseria G E and Ernzerhof M 2006 *J. Chem. Phys.* **124** 219906
- [71] Vydrov O A, Heyd J, Krukau A V and Scuseria G E 2006 *J. Chem. Phys.* **125** 074106
- [72] Martin R M 2004 *Electronic Structure: Basic Theory and Practical Methods* (Cambridge: Cambridge University Press)
- [73] Rydberg H, Dion M, Jacobson N, Schröder E, Hyldgaard P, Simak S I, Langreth D C and Lundqvist B I 2003 *Phys. Rev. Lett.* **91** 126402
- [74] Dion M, Rydberg H, Schröder E, Langreth D C and Lundqvist B I 2004 *Phys. Rev. Lett.* **92** 246401
- [75] Klimeš J, Bowler D R and Michaelides A 2011 *Phys. Rev. B* **83** 195131
- [76] Bučko T, Lebègue S, Hafner J and Ángyán J G 2013 *Phys. Rev. B* **87** 064110
- [77] Sun J *et al* 2016 *Nat. Chem.* **8** 831–6
- [78] Grimme S 2006 *J. Comput. Chem.* **27** 1787–99
- [79] Grimme S, Antony J, Ehrlich S and Krieg H 2010 *J. Chem. Phys.* **132** 154104
- [80] Grimme S, Ehrlich S and Goerigk L 2011 *J. Comput. Chem.* **32** 1456–65
- [81] Tkatchenko A, DiStasio R A, Car R and Scheffler M 2012 *Phys. Rev. Lett.* **108** 236402
- [82] Perdew J P and Zunger A 1981 *Phys. Rev. B* **23** 5048–79
- [83] Svane A and Gunnarsson O 1990 *Phys. Rev. Lett.* **65** 1148–51
- [84] Filippetti A and Spaldin N A 2003 *Phys. Rev. B* **67** 125109

- [85] Filippetti A and Spaldin N A 2003 *Phys. Rev. B* **68** 045111
- [86] Pemmaraju C D, Archer T, Sánchez-Portal D and Sanvito S 2007 *Phys. Rev. B* **75** 045101
- [87] Silveira O J and Chacham H 2017 *J. Phys.: Condens. Matter* **29** 09LT01
- [88] Droghetti A, Pemmaraju C D and Sanvito S 2008 *Phys. Rev. B* **78** 140404
- [89] Droghetti A and Sanvito S 2009 *Appl. Phys. Lett.* **94** 252505
- [90] Anisimov V I, Aryasetiawan F and Lichtenstein A I 1997 *J. Phys.: Condens. Matter* **9** 767
- [91] Campo V L Jr and Cococcioni M 2010 *J. Phys.: Condens. Matter* **22** 055602
- [92] Moore K T and van der Laan G 2009 *Rev. Mod. Phys.* **81** 235–98
- [93] Blöchl P E 1994 *Phys. Rev. B* **50** 17953–79
- [94] Kresse G and Joubert D 1999 *Phys. Rev. B* **59** 1758–75
- [95] Belsky A, Hellenbrandt M, Karen V L and Luksch P 2002 *Acta Crystallogr. B* **58** 364–9
- [96] Roth W L 1958 *Phys. Rev.* **110** 1333–41
- [97] McKay J M and Henrich V E 1985 *Phys. Rev. B* **32** 6764–72
- [98] Franchini C, Bayer V, Podloucky R, Paier J and Kresse G 2005 *Phys. Rev. B* **72** 045132
- [99] Schrön A, Rödl C and Bechstedt F 2012 *Phys. Rev. B* **86** 115134
- [100] Samsonov G V 1973 *The Oxide Handbook* (New York: IFI)
- [101] Kubaschewski O, Alcock C B and Spencer P J 1993 *Materials Thermochemistry* (Oxford: Pergamon)
- [102] Paier J, Marsman M, Hummer K, Kresse G, Gerber I C and Ángyán J G 2006 *J. Chem. Phys.* **124** 154709
- [103] Franchini C, Podloucky R, Paier J, Marsman M and Kresse G 2007 *Phys. Rev. B* **75** 195128
- [104] Hummer K, Grüneis A and Kresse G 2007 *Phys. Rev. B* **75** 195211
- [105] Paier J, Marsman M and Kresse G 2008 *Phys. Rev. B* **78** 121201
- [106] Chevrier V L, Ong S P, Armiento R, Chan M K Y and Ceder G 2010 *Phys. Rev. B* **82** 075122
- [107] Chen J, Wu X and Selloni A 2011 *Phys. Rev. B* **83** 245204
- [108] Yan J and Nørskov J K 2013 *Phys. Rev. B* **88** 245204
- [109] Aras M and Kiliç c 2014 *J. Chem. Phys.* **141** 044106
- [110] Mook H A 1966 *Phys. Rev.* **148** 495–501
- [111] Alperin H A 1962 *J. Phys. Soc. Japan B* **17** 12
- [112] McNatt J L 1969 *Phys. Rev. Lett.* **23** 915–8
- [113] Fender B E F, Jacobson A J and Wedgwood F A 1968 *J. Chem. Phys.* **48** 990–4
- [114] Powell R J and Spicer W E 1970 *Phys. Rev. B* **2** 2182–93
- [115] Cheetham A K and Hope D A O 1983 *Phys. Rev. B* **27** 6964–7
- [116] Hüfner S, Osterwalder J, Riesterer T and Hulliger F 1984 *Solid State Commun.* **52** 793–6
- [117] Rohrbach A, Hafner J and Kresse G 2004 *Phys. Rev. B* **69** 075413
- [118] Carpenter M K and Corrigan D A 1989 *J. Electrochem. Soc.* **136** 1022–6
- [119] Varkey A J and Fort A F 1993 *Thin Solid Films* **235** 47–50
- [120] Guzmán R S S, Vilche J R and Arvía A J 1978 *Corros. Sci.* **18** 765–78
- [121] Melendres C A and Xu S 1984 *J. Electrochem. Soc.* **131** 2239–43
- [122] Hoppe H W and Strehblow H H 1990 *Corros. Sci.* **31** 167–77
- [123] Druska P, Strehblow H H and Golledge S 1996 *Corros. Sci.* **38** 835–51
- [124] Druska P and Strehblow H H 1996 *Corros. Sci.* **38** 1369–83
- [125] Lo Y L and Hwang B J 1998 *Langmuir* **14** 944–50
- [126] Lillard R S and Scully J R 1998 *J. Electrochem. Soc.* **145** 2024–32
- [127] Han S Y, Lee D H, Chang Y J, Ryu S O, Lee T J and Chang C H 2006 *J. Electrochem. Soc.* **153** C382–6
- [128] Sun J, Ruzsinszky A and Perdew J P 2015 *Phys. Rev. Lett.* **115** 036402
- [129] Warschkow O, Wang Y, Subramanian A, Asta M and Marks L D 2008 *Phys. Rev. Lett.* **100** 086102
- [130] Yin W, Wolf S, Ko C, Ramanathan S and Reinke P 2011 *J. Appl. Phys.* **109** 024311
- [131] Bert J A, Kalisky B, Bell C, Kim M, Hikita Y, Hwang H Y and Moler K A 2011 *Nat. Phys.* **7** 767–71
- [132] Buschow K, van Engen P and Jongebreur R 1983 *J. Magn. Mater.* **38** 1–22
- [133] Katayama T, Suzuki Y, Awano H, Nishihara Y and Koshizuka N 1988 *Phys. Rev. Lett.* **60** 1426–9